Numerical simulation of bubble dynamics in the gravitational and uniform electric fields

Yanning Wang, Dongliang Sun, Aolin Zhang & Bo Yu

Taylor & Francis
Taylor & Francis Group

Check for updates

Numerical simulation of bubble dynamics in the gravitational and uniform electric fields

Yanning Wang[a,b], Dongliang Sun[a,b], Aolin Zhang[c], and Bo Yu[a]

[a]School of Mechanical Engineering, Beijing Institute of Petrochemical Technology, Beijing, China; [b]School of Renewable Energy, North China Electric Power University, Beijing, China; [c]College of Mechanical and Electrical Engineering, Beijing University of Chemical Technology, Beijing, China

ABSTRACT

A coupled volume-of-fluid, level set, and smoothed physical parameter (VOF+LS+SPP) method based on FLUENT is used to simulate bubble dynamics in the gravitational and uniform electric fields. Both of the bubble and surrounding medium are assumed to be perfect dielectrics with constant but different permittivities. The effects of electric Bond number, permittivity ratio, Morton number, and Eotvos number on the deformation and rising motion of a single bubble are systematically investigated. Simulation results show that a vertical electric field elongates the bubble along the electric field direction and accelerates the bubble rising. The electric Bond number has a much greater effect on bubble deformation and rising velocity than the permittivity ratio. The bubble behaviors in the electric field are similar for different Morton numbers but totally different for various Eotvos numbers. The influence of electric field on bubble Reynolds number changes a little for different Morton numbers but decreases distinctly with the increase of Eotvos number.

1. Introduction

The behaviors of a single bubble ascending in another viscous fluid play an indispensable role in many industrial applications, such as chemical engineering, energy and power engineering, gas–liquid column reactors, and waste water treatment. Bubble dynamics in the gravitational field have been investigated by plenty of scholars using experimental methods [1–4]. Grace [1] analyzed a large amount of experimental data given by different investigators and provided a general graphic correlation, which makes it possible to predict the terminal shape and rising velocity of a single bubble based on the fluid properties. Bhaga and Weber [2] conducted a series of detailed experiments which covered a large range of Reynolds and Morton numbers, and observed different bubble shapes with different terminal velocities. Experimental results of Wu and Gharib [3] showed that the shape of a small air bubble rising in clean water makes a great difference to its rising velocity and path. A large number of experimental data offer great convenience to verify the numerical simulation results and stimulate the study on bubble dynamics with different numerical methods [5–11]. Van Sint Annaland et al. [5] simulated the dynamics of a single bubble and the coalescence of two coaxial or oblique bubbles by a three-dimensional volume-of-fluid (VOF) method. Amaya-Bower and Lee [6] gave a comprehensive study about the deformation, motion, and pressure distribution of a bubble using a lattice Boltzmann method. Yu and Fan [8] applied a three-dimensional level set (LS) method to the investigation of rising bubbles with different shapes in infinite liquid. Ohta et al. [11] investigated

Nomenclature

A	dimensionless largest horizontal cross-section of bubble		$\boldsymbol{u}$	velocity vector, m/s
B	maximum bubble width, m		u_∞	terminal bubble rising velocity, m/s
$\mathrm{Bo_e}$	electric Bond number		u_z	velocity along the z-direction, m/s
Co	Courant number		U	dimensionless average bubble rising velocities
d	distance from interface, m		y_b	bubble bottom position, m
D	deformation rate		α	volume fraction
$\boldsymbol{E}$	electric field intensity, N/C		ϕ	electric potential, V
Eo	Eotvos number		$\delta(\varphi)$	Dirac distribution function
$\boldsymbol{F_\sigma}$	surface tension, N/m³		ε	relative permittivity
$\boldsymbol{F_e}$	electric field force, N/m³		ε_0	permittivity of vacuum, F/m
$\boldsymbol{g}$	gravitational acceleration, m/s²		λ_ε	permittivity ratio
$H(\varphi)$	Heaviside function		λ_μ	viscosity ratio
$\kappa(\varphi)$	interface curvature, m⁻¹		λ_ρ	density ratio
L	maximum bubble length, m		μ	fluid dynamic viscosity, Pa · s
M	Morton number		ρ	fluid density, kg/m³
p	pressure, Pa		σ	surface tension coefficient, N/m
$\boldsymbol{r}$	position vector, m		φ	level set function, m
R	bubble radius, m		Δ	grid size, m
Re	Reynolds number			
t	time, s		***Subscripts***	
T	dimensionless time		g	gas phase
			l	liquid phase

the influence of initial bubble conditions on the final deformation and motion of a bubble by a two-dimensional axisymmetric coupled LS and VOF (CLSVOF) method. All of the researches have shown that the bubble dynamics are fully determined by physical properties of the bubble and its surrounding fluid.

In order to manipulate the motion and deformation of bubbles, it is necessary to exert an external force, which can be easily controlled, during the motion of bubble. In recent years, the method of imposing an external electric field to adjust the rising bubble has become a hot research subject. Sarnobat et al. [12] experimentally studied the effect of an external electrostatic field on the formation of nitrogen bubbles from a single nozzle in glycerol. Dong et al. [13] experimentally investigated the influence of a uniform direct current electric field on the evolution and detachment of a bubble attached to the wall. Di Bari and Robinson [14] mainly focused on the deformation and stress distribution of a single adiabatic bubble growing in HFE-7000 in their experiment. Besides, a large amount of numerical simulations have also been performed. By using the VOF method, Zhang et al. [15] presented their simulation results that the existence of an electric field enhances the heat transfer around the bubble and elongates the bubble along the electric field direction in nucleate boiling process. Shin [16] simulated the rising process of a bubble in another liquid with top free surface using a level contour reconstruction method. Di Marco et al. [17] utilized a combination of the LS and VOF methods, along with the ghost fluid method, to predict the bubble deformation in the gravitational and electric fields. Sunder and Tomar [18] obtained an interesting conclusion that a non-uniform electric field with appropriate electrode configurations is a useful means to reduce the volume of bubbles detached from submerged needles by a CLSVOF method. Later, Sunder and Tomar [19] investigated the effects of an alternating current electric field on bubble dynamics. Generally speaking, all above researches were concentrated on the growth and detachment of a bubble adhered to the wall or nozzle.

The rising motion of bubbles in the gravitational and electric fields has also been studied by some scholars. Mählmann and Papageorgiou [20] applied the LS method to investigate the motion of a two-dimensional bubble. Results showed that the existence of an electric field reduces the deformations and oscillations of bubble shapes and hinders the bubble breakage effectively. Yang et al. [21, 22] simulated the different effects of vertical and horizontal external electric fields on the bubble rising

in another viscous fluid using a three-dimensional phase field model and found that an external electric field stretches the bubble along the electric field direction. It was resulted that a vertical electric field accelerates the ascending of bubble, while a horizontal one decelerates it. Wang et al. [23] investigated the dynamic behaviors of a single bubble subjected to a uniform electric field with a three-dimensional coupled VOF and LS (VOSET) method. They discovered the same phenomena as Yang et al. [21, 22] when a bubble was subjected to a vertical electric field. An electric field which is gradually added at a different time can effectively prevent the break-up of bubble. Later, the bubble dynamics in the microgravity and non-uniform electric field were investigated [24]. Results showed that the existence of a non-uniform electric field accelerates the bubble rising velocity. However, researches on the motion and deformation of rising bubbles are still limited.

In this paper, the influence of an external electric field on the dynamics of an initially spherical bubble with different Morton and Eotvos numbers are systematically investigated. In addition, most scholars developed their own program codes to investigate the bubble dynamics in the electric field. It is difficult to be mastered by other scholars. Therefore, it is a good choice to use the commercial software FLUENT. With the help of user-defined scalars (UDSs) and user-defined functions (UDFs) provided by FLUENT, a coupled VOF, LS, and smoothed physical parameter (VOF+LS+SPP) method [25], which was proposed by the present authors, is used to solve this problem.

2. Governing equations and numerical method

2.1. Governing equations

The bubble deformation and motion processes in the gravitational and electric fields are considered to be incompressible, laminar, and unsteady two-phase flow problems. They are governed by the coupled inertial force, viscous force, gravity, surface tension, and electric field force. The mass and momentum conservation equations are expressed as

$$\nabla \cdot \boldsymbol{u} = 0 \tag{1}$$

$$\frac{\partial(\rho \boldsymbol{u})}{\partial t} + \nabla \cdot (\rho \boldsymbol{u}\boldsymbol{u}) = -\nabla p + \nabla \cdot \left[\mu\left(\nabla \boldsymbol{u} + \nabla \boldsymbol{u}^{\mathrm{T}}\right)\right] + \rho \boldsymbol{g} + \boldsymbol{F}_{\sigma} + \boldsymbol{F}_{e} \tag{2}$$

where $\boldsymbol{u}$ is the velocity vector, ρ is the density, t is the time, p is the pressure, μ is the dynamic viscosity, $\boldsymbol{g}$ is the gravitational acceleration, $\boldsymbol{F}_{\sigma}$ and $\boldsymbol{F}_{e}$ are the surface tension and electric field force, respectively.

2.2. Perfect dielectric model

Under the assumption that the electric conductivities of two fluids could be neglected, there are no free charges throughout the whole space. The electric field intensity satisfies

$$\nabla \cdot (\varepsilon_0 \varepsilon \boldsymbol{E}) = 0 \tag{3}$$

where $\boldsymbol{E}$ is the electric field intensity, ε_0 is the permittivity of vacuum, and ε is the relative permittivity.

In electrohydrodynamics, the dynamic current is so small that the magnetic induction can be ignored, which means that the electric field intensity is irrotational [26].

$$\nabla \times \boldsymbol{E} = 0 \tag{4}$$

Therefore, the electric field intensity can be expressed as the gradient of electric potential ϕ.

$$\boldsymbol{E} = -\nabla \phi \tag{5}$$

Combining Eqs. (3) and (5), it can be obtained that

$$\nabla \cdot (\varepsilon_0 \varepsilon \nabla \phi) = 0 \tag{6}$$

The electric field force can be calculated by [23]

$$F_e = -\frac{1}{2}\varepsilon_0[(-\nabla\phi)\cdot(-\nabla\phi)]\nabla\varepsilon \tag{7}$$

It is obvious that the electric field force only acts perpendicularly to the interface for two uniformly distributed mediums.

2.3. VOF+LS+SPP method

The details of the VOF+LS+SPP method have been well-documented in Reference [25], and a simple introduction is presented here. The piecewise linear interface construction (PLIC) algorithm in VOF method [27] is used to calculate the volume fractions of different phases in each grid cell. The value of volume fraction α lies between 0 and 1. When $0 < \alpha < 1$, the grid cell contains the phase interface. For a gas–liquid two-phase flow system, the sum of volume fractions of two phases in each grid cell satisfies

$$\alpha_g + \alpha_l = 1 \tag{8}$$

where the subscripts g and l refer to gas and liquid phases, respectively.

The transport equation of gas volume fraction can be written as follows.

$$\frac{\partial\alpha_g}{\partial t} + \nabla\cdot\left(u\alpha_g\right) = 0 \tag{9}$$

The LS function φ [28] is introduced to calculate the surface tension. φ is defined as a signed distance to the interface. It is greater than zero in the liquid phase, while the symbol is opposite in the gas phase and it equals zero on the interface.

$$\varphi(r, t) = \begin{cases} +|d| & r \in \text{the liquid phase} \\ 0 & r \in \text{the interface} \\ -|d| & r \in \text{the gas phase} \end{cases} \tag{10}$$

where r is the position vector, and d is the distance from interface.

The evolution of LS function is given as

$$\frac{\partial\varphi}{\partial t} + u\cdot\nabla\varphi = 0 \tag{11}$$

According to the continuum surface force (CSF) model [29], the surface tension F_σ can be expressed as

$$F_\sigma = -\sigma\kappa(\varphi)\delta(\varphi)\nabla\varphi \tag{12}$$

where σ is the surface tension coefficient and the interface curvature $\kappa(\varphi)$ is obtained from

$$\kappa(\varphi) = \nabla\cdot\left(\frac{\nabla\varphi}{|\nabla\varphi|}\right) \tag{13}$$

$\delta(\varphi)$ is the Dirac distribution function and defined as

$$\delta(\varphi) = \begin{cases} \frac{1+\cos(\pi\varphi/\gamma)}{2\gamma} & |\varphi| \leq \gamma \\ 0 & |\varphi| > \gamma \end{cases} \tag{14}$$

where $\gamma = 1.5\Delta$, and Δ denotes the grid size.

The density, dynamic viscosity, and permittivity are calculated by the volume fraction α in the default VOF+LS method in FLUENT. However, because the volume fraction α is a step function, it is difficult to smooth the discontinuous physical parameters near the interface, decreasing the accuracy of numerical results. To overcome this disadvantage, with the help of UDFs in the FLUENT

software, the LS function φ is used to obtain the smoothed physical parameters (SPP).

$$\rho = \rho_g(1 - H(\varphi)) + \rho_l H(\varphi) \tag{15}$$

$$\mu = \mu_g(1 - H(\varphi)) + \mu_l H(\varphi) \tag{16}$$

$$\varepsilon = \varepsilon_g(1 - H(\varphi)) + \varepsilon_l H(\varphi) \tag{17}$$

where $H(\varphi)$ is the Heaviside function and defined as

$$H(\varphi) = \begin{cases} 0 & \varphi < -\gamma \\ \frac{1}{2}\left[1 + \frac{\varphi}{\gamma} + \frac{1}{\pi}\sin\left(\frac{\pi\varphi}{\gamma}\right)\right] & |\varphi| \leq \gamma \\ 1 & \varphi > \gamma \end{cases} \tag{18}$$

2.4. Numerical details

The PISO algorithm is used to couple the velocity and pressure [Eqs. (1) and (2)]. The second-order upwind scheme is adopted for convection term in the momentum and LS equations [Eqs. (2) and (11)]. Equation (6) is solved by using the UDS in FLUENT software. The electric field force [Eq. (7)] and smoothed physical parameters (SPP) [Eqs. (15–17] are calculated by using the developed UDFs. The governing equation of volume fraction [Eq. (9)] is solved by the PLIC algorithm in the VOF method. The first-order implicit scheme treats the time marching. The time step Δt is controlled by a specified maximum value for the Courant number, which is defined as

$$Co = \frac{\Delta t}{\Delta / |\boldsymbol{u}|} \tag{19}$$

where $|\boldsymbol{u}|$ is the fluid velocity within the grid. The Courant number is set to be $Co \leq 0.02$.

3. Physical problem and verification

3.1. Physical problem

The physical problem for the simulation is shown in Figure 1. A spherical bubble with a radius R is initially located in the position (0, 3R) of a cylindrical domain. The domain has a size of 5R in r-direction and 22R in z-direction, as shown in Figure 1a. Due to the symmetry of geometry and flow structures, an axial-symmetric coordinate system $r–z$ is used to perform the numerical simulations. Figure 1b shows the corresponding computational region and boundary conditions. The axial-symmetric velocity boundary condition is used at the left boundary, and the no-slip velocity boundary condition is applied at other boundaries. The electric potentials of top and bottom boundaries are set as ϕ_0 and 0, respectively, while a Neumann boundary condition is applied at other boundaries. Thus, a uniform direct current electric field is generated along the z-direction.

3.2. Method verification

To verify the accuracy of numerical method, the deformation of a perfect dielectric bubble in the uniform direct current electric field and the rising motion of a bubble in the gravitational field are studied.

3.2.1. Deformation of a perfect dielectric bubble in a uniform electric field

The physical problem is similar to Figure 1 with just a little distinction. Here a spherical bubble with a radius R is initially located in the position (0, 5R) of a cylindrical domain. The domain has a size of 5R in r-direction and 10R in z-direction. Both bubble and external liquid are assumed to be homogeneous and have the same density and viscosity. Sherwood [30] pointed out that the bubble
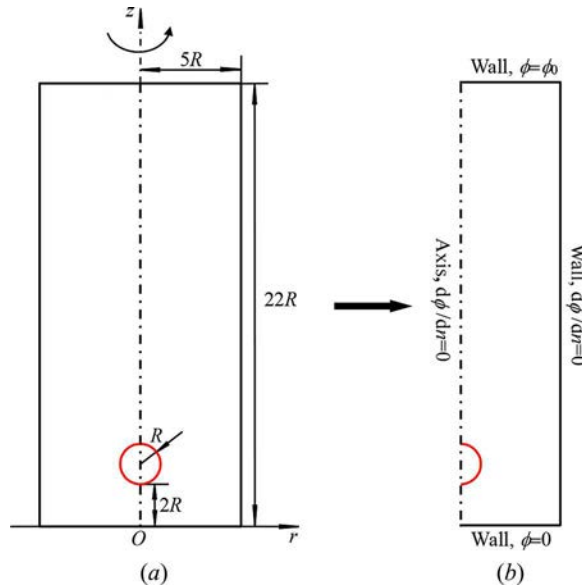
Figure 1. Physical problem of the bubble dynamics in the gravitational and uniform direct current electric fields: (a) schematic diagram, (b) computational region.

deformation can be fully decided by

$$\mathrm{Bo_e} = \frac{\varepsilon_0 \varepsilon_l |E_0|^2 R}{\sigma}, \ \lambda_\varepsilon = \frac{\varepsilon_l}{\varepsilon_g} \tag{20}$$

where E_0 denotes the electric field intensity without the bubble. The magnitude of E_0 is $\phi_0/10R$ in this case. The electric Bond number ($\mathrm{Bo_e}$) describes the relative importance between the electric field force and surface tension. λ_ε represents the permittivity ratio between the liquid and gas phases.

A grid independence test is performed using three different grid systems. The grid systems are chosen to be $100(r) \times 200(z)$, $140(r) \times 280(z)$, and $200(r) \times 400(z)$, respectively. The electric Bond number is equal to 0.5, while the permittivity ratio is set to be 0.2. As shown in Figure 2, simulation results are almost the same for three different grid systems. Thus, the grid system is chosen to be $100(r) \times 200(z)$ in the following simulations.

As shown in Figure 2, the bubble will be elongated along the electric field direction and takes the form of a prolate spheroid. To give a quantitative description of the bubble deformation,
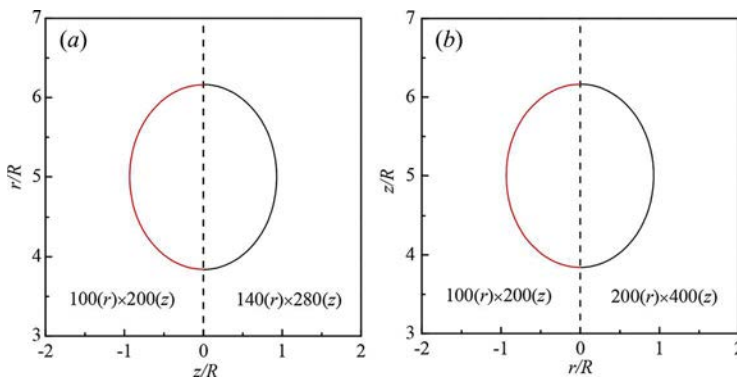

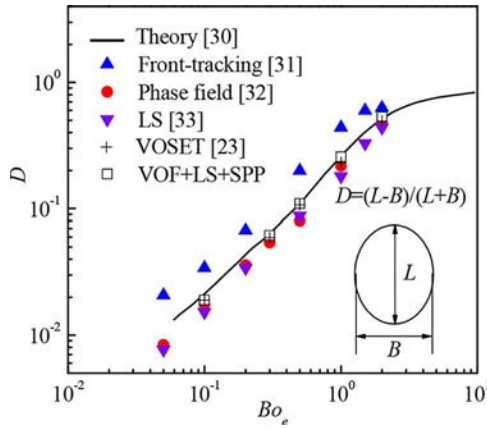**Figure 2.** Terminal shapes of a perfect dielectric bubble for three different grid systems when $\mathrm{Bo_e} = 0.5$ and $\lambda_\varepsilon = 0.2$.

Figure 3. Bubble deformation rates (D) with different electric Bond numbers (Bo_e) when $\lambda_\varepsilon = 0.2$.

the deformation rate D is introduced and its definition is shown in Figure 3. Figure 3 shows the bubble deformation rates with different electric Bond numbers when $\lambda_\varepsilon = 0.2$. It can be seen that the results obtained by VOF+LS+SPP method give a nearly direct match with the theoretical curve. Current simulation results are as accurate as results given by VOSET method [23], and more accurate than other results given by available literatures [31–33].

3.2.2. Bubble dynamics in a gravitational field

The physical problem is exactly the same as Figure 1 except the absence of electric field. According to Grace [1], the deformation and motion of a single bubble in the gravitational field can be fully described by four dimensionless numbers, including the Morton number (M), the Eotvos number (Eo), the viscosity ratio (λ_μ), and the density ratio (λ_ρ).

$$M = \frac{|\mathbf{g}|\mu_l^4}{\rho_l\sigma^3}, \quad Eo = \frac{4|\mathbf{g}|R^2\left(\rho_l - \rho_g\right)}{\sigma}, \quad \lambda_\mu = \frac{\mu_l}{\mu_g}, \quad \lambda_\rho = \frac{\rho_l}{\rho_g} \tag{21}$$

The Morton number describes the relative importance between the viscous force and surface tension. The Eotvos number describes the relative importance between the buoyancy and surface tension. It can be derived that

$$\frac{Eo^{3/4}}{M^{1/4}} = \frac{\left(\rho_l - \rho_g\right)\sqrt{8R^3|\mathbf{g}|}\sqrt{\frac{\rho_l}{\rho_l - \rho_g}}}{\mu_l} \tag{22}$$

The value of $Eo^{3/4}/M^{1/4}$ describes the relative importance between the buoyancy and viscous force.

A grid independence test is performed using three different grid systems. The grid systems are chosen to be $70(r) \times 308(z)$, $100(r) \times 440(z)$, and $140(r) \times 616(z)$, respectively. The four dimensionless numbers are set to be $M = 1,000$, $Eo = 97.1$, $\lambda_\mu = 100$, and $\lambda_\rho = 100$, respectively. As shown in Figure 4, simulation results are almost the same for three different grid systems. Thus, the grid system is chosen to be $100(r) \times 440(z)$ in the following simulations. In this paper, the dimensionless time T is defined as

$$T = \frac{t}{\sqrt{R/|\mathbf{g}|}} \tag{23}$$

Figure 5 shows the terminal shapes of a single bubble with different Morton and Eotvos numbers when $\lambda_\mu = 100$ and $\lambda_\rho = 100$. Figures 5a1–5c1 are the simulation results given by Van Sint Annaland
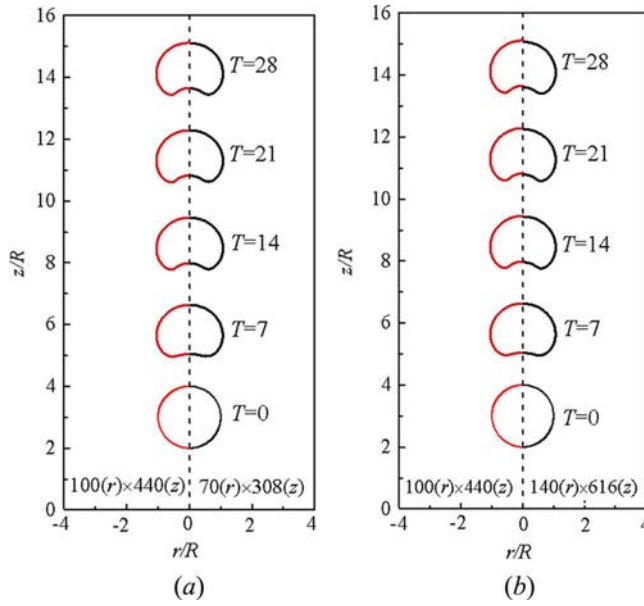
Figure 4. Evolution of the bubble shapes with time for three different grid systems when $M = 1000$, $Eo = 97.1$, $\lambda_\mu = 100$, and $\lambda_\rho = 100$.
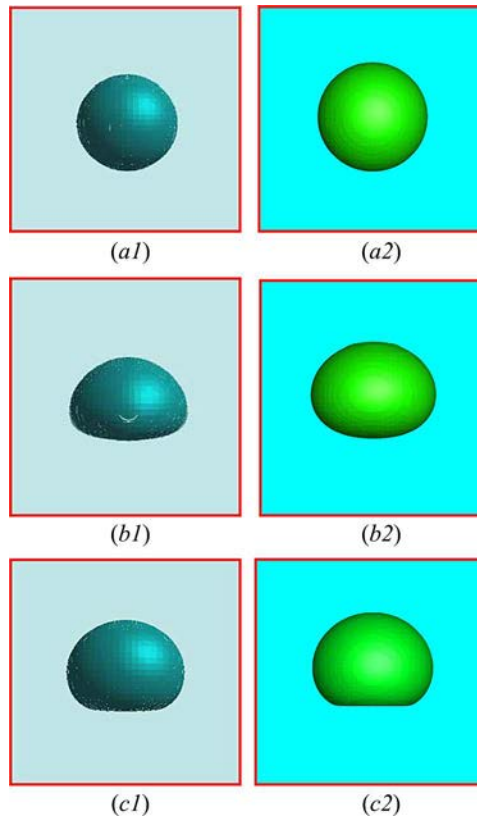

Figure 5. Terminal shapes of a single bubble with different Morton and Eotvos numbers when $\lambda_\mu = 100$ and $\lambda_\rho = 100$: (a1) and (a2) spherical: $M = 0.00126$, $Eo = 0.971$; (b1) and (b2) Ellipsoidal: $M = 0.1$, $Eo = 9.71$; (c1) and (c2) Dimpled/ellipsoidal: $M = 1000$, $Eo = 97.1$. (a1), (b1), and (c1) are simulation results given in literature [5]. (a2), (b2), and (c2) are the current simulation results.

Table 1. Bubble Reynolds numbers (Re) with different Morton (*M*) and Eotvos numbers (*Eo*).

Case	*M*	*Eo*	Re$_G$ [1]	Re$_A$ [5]	Re$_C$
1	0.00126	0.971	1.7	1.6	1.64
2	0.1	9.71	4.6	4.3	4.50
3	1,000.0	97.1	1.5	1.7	1.57

et al. [5] who used the three-dimensional VOF method. Figures 5a2–5c2 are current simulation results, which are almost the same as results of Van Sint Annaland et al.

The bubble Reynolds number is defined as

$$\text{Re} = \frac{2\rho_l u_\infty R}{\mu_l} \tag{24}$$

where u_∞ represents the terminal bubble rising velocity.

The corresponding Reynolds numbers for different cases are shown in Table 1. Re$_G$ are the experimental results given by Grace [1], Re$_A$ are the simulation results given by Van Sint Annaland et al. [5], and Re$_C$ represent current simulation results. Compared with results of Van Sint Annaland et al., current simulation results realize a closer match to the experimental results.

4. Results and discussion

In this section, the bubble dynamics in the combined gravitational and vertical uniform direct current electric fields are studied. By combining Eqs. (20) and (21), the bubble behaviors in the gravitational and uniform electric fields can be fully characterized by the following dimensionless parameters.

$$M = \frac{|\mathbf{g}|\mu_l^4}{\rho_l \sigma^3}, \text{Eo} = \frac{4|\mathbf{g}|R^2\left(\rho_l - \rho_g\right)}{\sigma}, \text{Bo}_e = \frac{\varepsilon_0 \varepsilon_l |\mathbf{E}_0|^2 R}{\sigma}, \lambda_\mu = \frac{\mu_l}{\mu_g}, \lambda_\rho = \frac{\rho_l}{\rho_g}, \lambda_\varepsilon = \frac{\varepsilon_l}{\varepsilon_g} \tag{25}$$

In the following simulations, the grid system is chosen to be $100(r) \times 440(z)$, and both viscosity ratio (λ_μ) and density ratio($\lambda\rho$) are set to be 100. The effects of Morton number (*M*), Eotvos number (*Eo*), electric Bond number (Bo$_e$), and permittivity ratio (λ_ε) on the bubble motion and deformation are investigated.

4.1. Effect of the electric field force

The bubble behaviors are investigated by changing the electric Bond number and permittivity ratio. Figure 6 shows the evolution of bubble shapes for different electric Bond numbers when $M = 0.1$, $Eo = 10$, and $\lambda_\varepsilon = 5$. It is obvious that the bubble experiences a deformation process within a short time ($T \leq 4$) and ascends steadily thereafter ($T > 4$) for different electric Bond numbers. For the bubble in the absence of electric field (Figure 6a), the bubble finally takes an ellipsoidal shape. Once the bubble is subjected to an electric field, it will be stretched along the electric field direction. A larger electric Bond number produces a greater deformation, higher rising velocity, and sharper bottom of the bubble, as shown in Figures 6b–6d. The influence of permittivity ratio on the evolution of bubble shapes is shown in Figure 7, when $M = 0.1$, $Eo = 10$, and Bo$_e = 5$. As can be seen from Figure 7, a larger permittivity ratio also realizes a greater deformation, higher rising velocity, and sharper bottom of the bubble.

However, the electric Bond number has a greater influence on the bubble deformation and rising motion than the permittivity ratio. By taking the bubble at $T = 10$ as an example, the bubble height has a pronounced increase when the electric Bond number increases (Figure 6), while the increase of permittivity ratio only has a little influence on the bubble height when $\lambda_\varepsilon \geq 10$ (Figure 7).
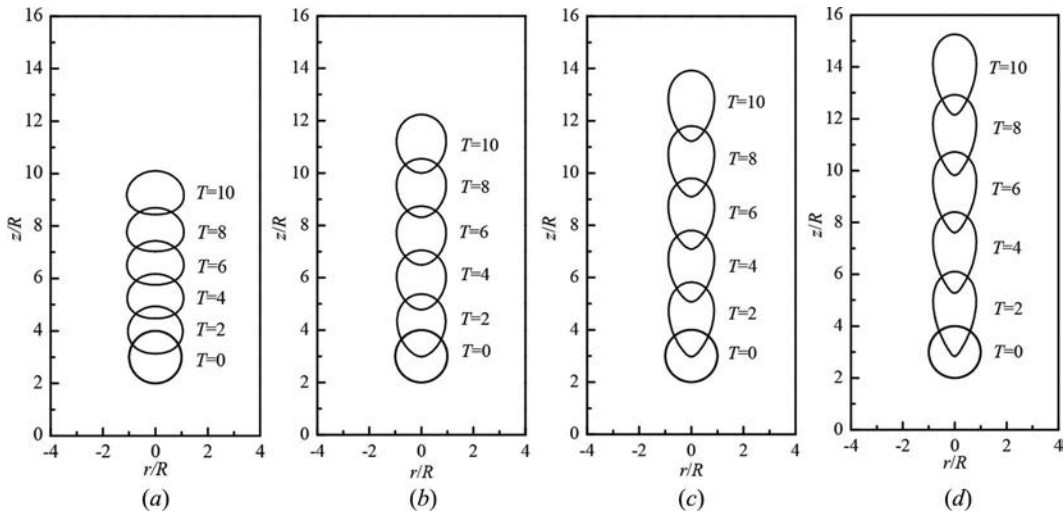
Figure 6. Evolution of the bubble shapes for different electric Bond numbers (Bo_e) when $M = 0.1$, $Eo = 10$, and $\lambda_\varepsilon = 5$: (a) $Bo_e = 0$, (b) $Bo_e = 5$, (c) $Bo_e = 10$, (d) $Bo_e = 15$.

The electric potential profiles when $M = 0.1$, $Eo = 10$, $Bo_e = 5$, and $\lambda_\varepsilon = 5$ are shown in Figure 8a. The electric potential profiles are more intensive at the bubble equator than the profiles at the poles. The electric field intensity is non-uniform around the interface. To be specific, the electric field intensity is higher at the bubble equator, while the weaker one is located at the poles. Furthermore, the permittivity of external liquid is greater than that of bubble when $\lambda_\varepsilon > 1$. It results that the permittivity gradient around the interface points toward the liquid. Under the combined effects of electric field intensity and permittivity gradient, the electric field force acts toward the inside of bubble, and the electric field force at the bubble equator is stronger than that at the poles, which produces a transverse compressive deformation of the bubble (Figure 8b). Finally, the bubble is stretched along the electric field direction and its largest horizontal cross-section is decreased. As a consequence, the bubble flow resistance reduces and its rising velocity increases. Figure 9 shows
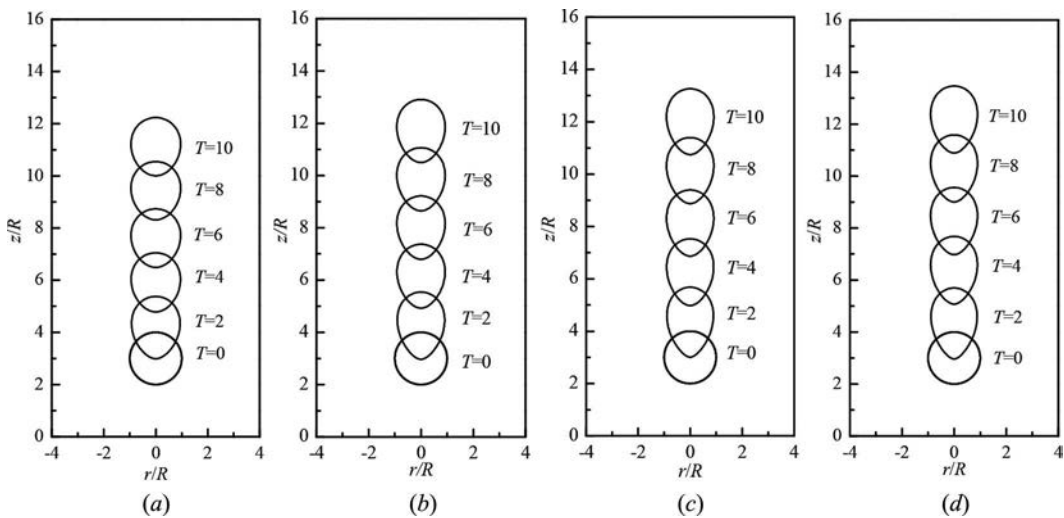

Figure 7. Evolution of the bubble shapes for different permittivity ratios (λ_ε) when $M = 0.1$, $Eo = 10$, and $Bo_e = 5$: (a) $\lambda_\varepsilon = 5$, (b) $\lambda_\varepsilon = 10$, (c) $\lambda_\varepsilon = 20$, (d) $\lambda_\varepsilon = 40$.
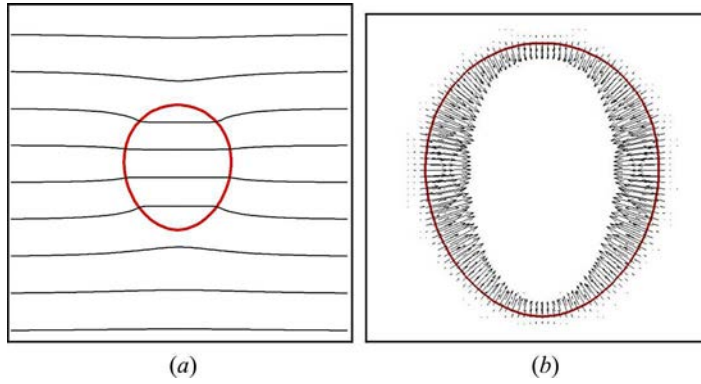
Figure 8. Electric potential and electric field force distributions when $M = 0.1$, $Eo = 10$, $Bo_e = 5$, and $\lambda_\varepsilon = 5$: (a) electric potential, (b) electric field force.

the bubble Reynolds numbers and dimensionless largest horizontal cross-sections for different electric Bond numbers and permittivity ratios when $M = 0.01$ and $Eo = 10$. The dimensionless largest horizontal cross-section is defined as

$$A = \frac{\pi B^2}{4\pi R^2} = \frac{B^2}{4R^2} \tag{26}$$

where B is the maximum bubble width. Figure 9a shows that the dimensionless largest horizontal cross-section decreases significantly with the increase of electric Bond number. Therefore, the bubble Reynolds number increases almost linearlly in this situation. There is only a slight decline for the growth rate of bubble Reynolds number. In addition, as shown in Figure 9b, because the dimensionless largest horizontal cross-section declines very slowly when $\lambda_\varepsilon \geq 10$, the Reynolds number increases only a little even for a great change of permittivity ratio.

4.2. Effect of Morton number

The bubble rising velocity is mainly decided by the buoyancy and viscous force. According to Eq. (22), the relative importance between the buoyancy and viscous force is inversely proportional to $M^{1/4}$. With the increase of Morton number, the buoyancy becomes weaker, while the viscous force becomes stronger, which causes the bubble rising velocity to decrease. The transient development of dimensionless average bubble rising velocities predicted by the numerical simulation when $Eo = 10$,
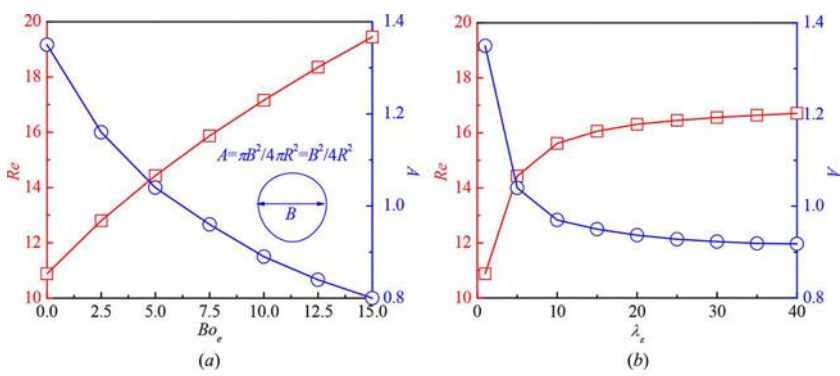

Figure 9. Bubble Reynolds numbers (Re) and dimensionless largest horizontal cross-sections (A) for different electric Bond numbers (Bo$_e$) and permittivity ratios (λ_ε) when $M = 0.01$, $Eo = 10$: (a) $\lambda_\varepsilon = 5$, (b) Bo$_e = 5$.
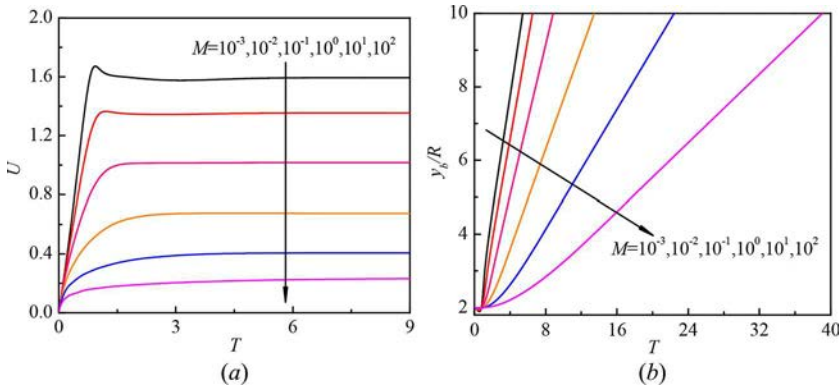
Figure 10. Transient development of (a) dimensionless average bubble rising velocities and (b) bubble bottom positions in the electric field when $Eo = 10$, $Bo_e = 10$, and $\lambda_\varepsilon = 5$.

$Bo_e = 10$, and $\lambda_\varepsilon = 5$ are shown in Figure 10a. The Morton number increases from 10^{-3} to 10^2 along the arrow direction. It can be seen that the dimensionless average bubble rising velocity decreases from 1.59 to 0.23. As a result, the bubble bottom position rises lower for larger Morton number, as shown in Figure 10b. In Figure 10, the bubble bottom position is represented by y_b. The dimensionless average bubble rising velocities U is obtained by

$$U = \frac{\int u_z \alpha_g d\tau}{\int \alpha_g d\tau} \Big/ \sqrt{|\mathbf{g}|R} \tag{27}$$

where u_z is the velocity along the z-direction and $\int d\tau$ represents the integral in the whole area.

Figure 11 shows the transient development of maximum bubble lengths for different Morton numbers when $Eo = 10$, $Bo_e = 10$, and $\lambda_\varepsilon = 5$. The maximum bubble length L is used to characterize the bubble deformation along the electric field direction. At first, the bubble rising velocity is small, its deformation is mainly influenced by the electric field force, surface tension, and viscous force. The bubble is stretched along the electric field direction. With the increase of Morton number, the viscous force increases and the deformation process is hindered. Therefore, the bubble deformation process is the fastest when $M = 10^{-3}$. However, after a little while, the bubble rising velocity reaches a certain value and its deformation is beginning to be greatly influenced by the inertia force. Figure 10 shows that the bubble rising velocity decreases with the increase of Morton number. As a result, the influence of inertia force decreases, promoting the bubble deformation along the electric field direction. The bubble deformation along the electric field direction is the largest when $M = 10^2$.
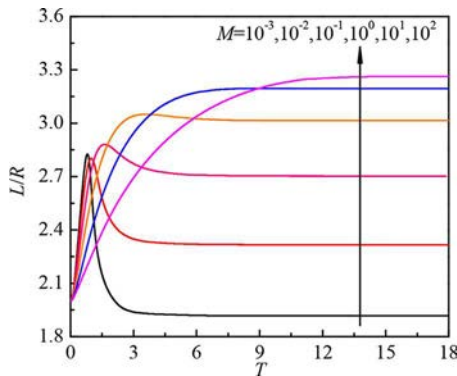

Figure 11. Transient development of the maximum bubble lengths L for different Morton numbers when $Eo = 10$, $Bo_e = 10$, and $\lambda_\varepsilon = 5$.

Figure 12a shows the relative bubble Reynolds numbers (Re_E/Re_0) for different Morton numbers when $Eo = 10$ and $\lambda_\varepsilon = 5$. Re_E and Re_0 denote the bubble Reynolds numbers with and without the electric field, respectively. The relative Reynolds number reflects the growth rate of the bubble Reynolds number under the action of an external electric field. From Figure 12a, it can be seen that the relative Reynolds number almost remains the same for different Morton numbers with other parameters unchanged. It is seen that the influence of electric field on bubble Reynolds number is insensitive to the variation of Morton number. As can be seen from Figure 12b, the results come from the relative dimensionless largest horizontal cross-section (A_E/A_0) fluctuates slightly nearby a constant value for different Morton numbers. Here, A_E and A_0 denote the dimensionless largest horizontal cross-sections with and without the electric field, respectively.

Figure 13 shows the terminal bubble shapes and velocity fields for different Morton and electric Bond numbers when $Eo = 10$ and $\lambda_\varepsilon = 5$. It is obvious that a larger velocity always corresponds to the smaller Morton number and larger electric Bond number. Besides, the bubble finally takes an ellipsoid when the Morton number is small (Figure 12a1), and the shape is gradually close to a sphere as the Morton number increases (Figures 12b1, c1). The existence of an electric field will produce a sharp bubble bottom (Figures 12a2–12c2). It can be seen that the bubble bottom becomes sharper with the increase of Morton number.

4.3. Effect of Eotvos number

According to Eq. (22), the relative importance between the buoyancy and viscous force is proportional to $Eo^{3/4}$. With the increase of Eotvos number, the buoyancy becomes stronger, while the viscous force becomes weaker, which causes the bubble rising velocity to increase. The transient development of dimensionless average bubble rising velocities predicted by the numerical simulation when $M = 10$, $Bo_e = 10$, and $\lambda_\varepsilon = 5$ are shown in Figure 14a. The Eotvos number increases from 2 to 100 along the arrow direction. It can be seen that the dimensionless average bubble rising velocity increases from 0.13 to 0.82. As a result, the bubble bottom position rises higher for larger Eotvos number, as shown in Figure 14b.

Figure 15 shows the transient development of maximum bubble lengths for different Eotvos numbers when $M = 10$, $Bo_e = 10$, and $\lambda_\varepsilon = 5$. The bubble deformation is mainly influenced by the electric field force, surface tension, viscous force, and inertia force. It can be seen in Figure 14 that the bubble rising velocity increases with the increase of the Eotvos number. As a result, the inertia force increases and the bubble deformation along the electric field direction is hindered. The bubble deformation along the electric field direction is the smallest when $Eo = 100$.
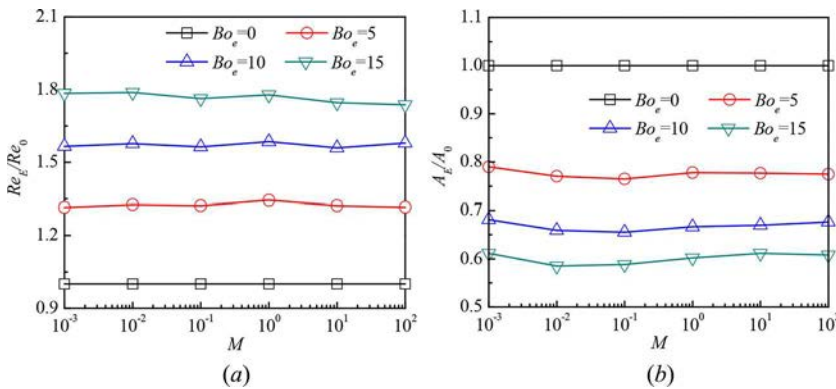

Figure 12. (a) Relative bubble Reynolds numbers (Re_E/Re_0) and (b) relative dimensionless largest horizontal cross-sections (A_E/A_0) for different Morton numbers (M) when $Eo = 10$ and $\lambda_\varepsilon = 5$.
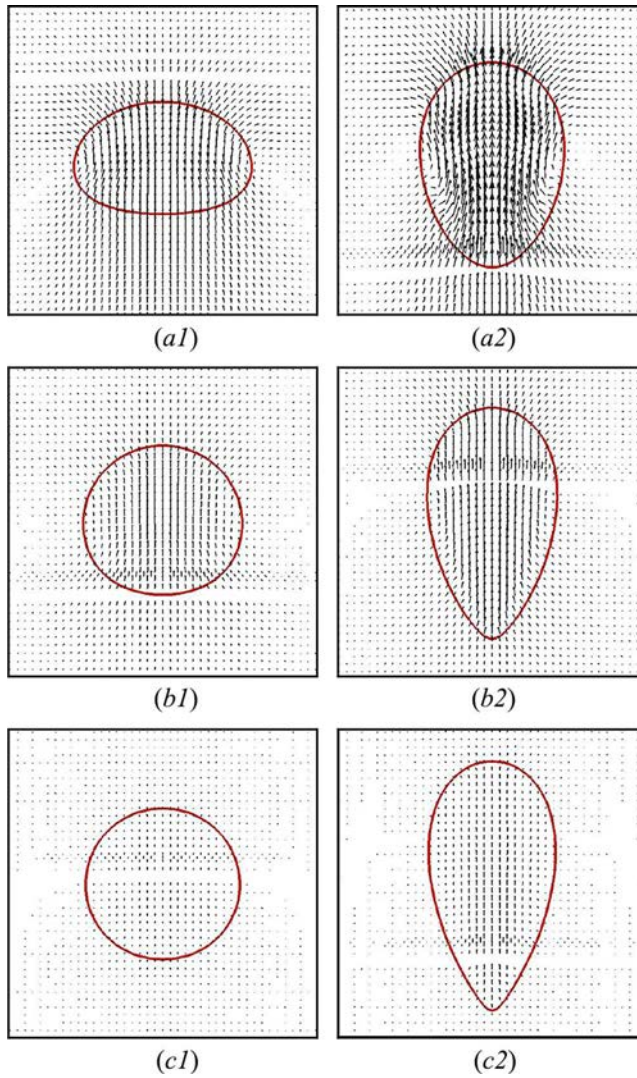
Figure 13. Terminal shapes and velocity fields of the bubble for different Morton numbers (M) and electric Bond numbers (Bo_e) when $Eo = 10$ and $\lambda_\varepsilon = 5$: (a1) $M = 10^{-2}$ and $Bo_e = 0$, (a2) $M = 10^{-2}$ and $Bo_e = 10$, (b1) $M = 10^0$ and $Bo_e = 0$, (b2) $M = 10^0$ and $Bo_e = 10$, (c1) $M = 10^2$ and $Bo_e = 0$, (c2) $M = 10^2$ and $Bo_e = 10$.
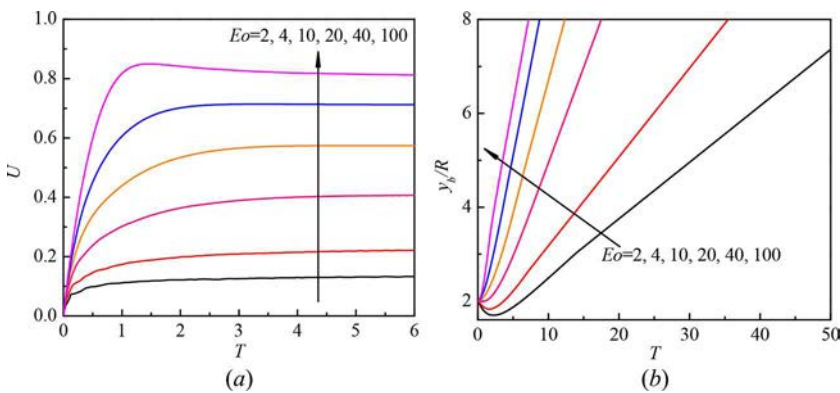

Figure 14. Transient development of (a) dimensionless average bubble rising velocities and (b) bubble bottom positions in the electric field when $M = 10$, $Bo_e = 10$, and $\lambda_\varepsilon = 5$.
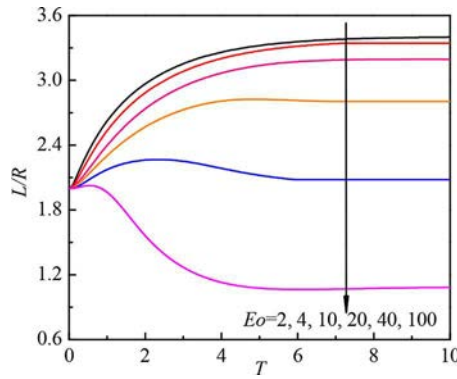
Figure 15. Transient development of the maximum bubble lengths L for different Eotvos numbers when $M = 10$, $Bo_e = 10$, and $\lambda_\varepsilon = 5$.

Figure 16a shows the relative bubble Reynolds numbers (Re_E/Re_0) for different Eotvos numbers when $M = 10$ and $\lambda_\varepsilon = 5$. It can be seen that the relative Reynolds number has a significant decrease with the increase of Eotvos number. For example, when the electric Bond number increases from 0 to 15, the values of Re_E/Re_0 are 1.00, 1.43, 1.74, and 2.08 for $Eo = 2$, while their values are only 1.00, 1.06, 1.12, and 1.18 for $Eo = 100$. As can be seen from Figure 16b, the results come from that the relative dimensionless largest horizontal cross-section (A_E/A_0) increases with the increase of Eotvos number. Finally, the resistance exerted on the bubble is enhanced and hinders the rising of bubble.

The Eotvos number describes the ratio between the buoyancy and surface tension. When the Eotvos number is small, the influence of buoyancy is small and the surface tension is dominated in the bubble deformation process. Once it is subjected to an electric field, the bubble deformation is mainly decided by the surface tension and electric field force. So, the bubble goes through a remarkable deformation and finally takes almost a prolate spheroid (Figure 17a2), which is similar to the bubble shape in a separate electric field (Figure 2). However, as the Eotvos number becomes larger, according to Wang et al. [23], the influence of buoyancy increases and wake flow becomes stronger. After imposing an electric field, the electric field force needs to overcome the stronger wake flow and the bubble experiences no significant change in the electric field, as shown in Figures 17c1, c2.

Besides, it is obvious that a larger velocity always corresponds to larger Eotvos and electric Bond numbers. The bubble with different Eotvos number has different shape when it is subjected to an electric field. When $Eo = 2$, the bubble finally takes a prolate spheroid in the electric field (Figure 17a2). When $Eo = 10$, the existence of an electric field will produce a sharp bubble bottom (Figure 17b2). When $Eo = 100$, the bubble in the electric field takes a dimpled ellipsoidal shape (Figure 17c2).
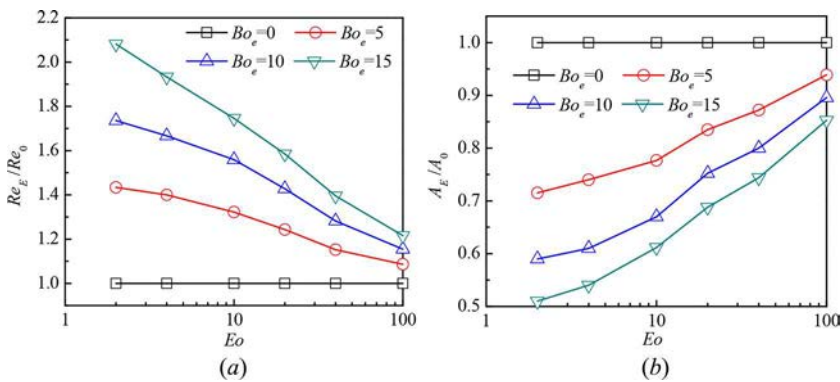

Figure 16. (a) Relative bubble Reynolds numbers (Re_E/Re_0) and (b) relative dimensionless largest horizontal cross-sections (A_E/A_0) for different Eotvos numbers (Eo) when $M = 10$ and $\lambda_\varepsilon = 5$.
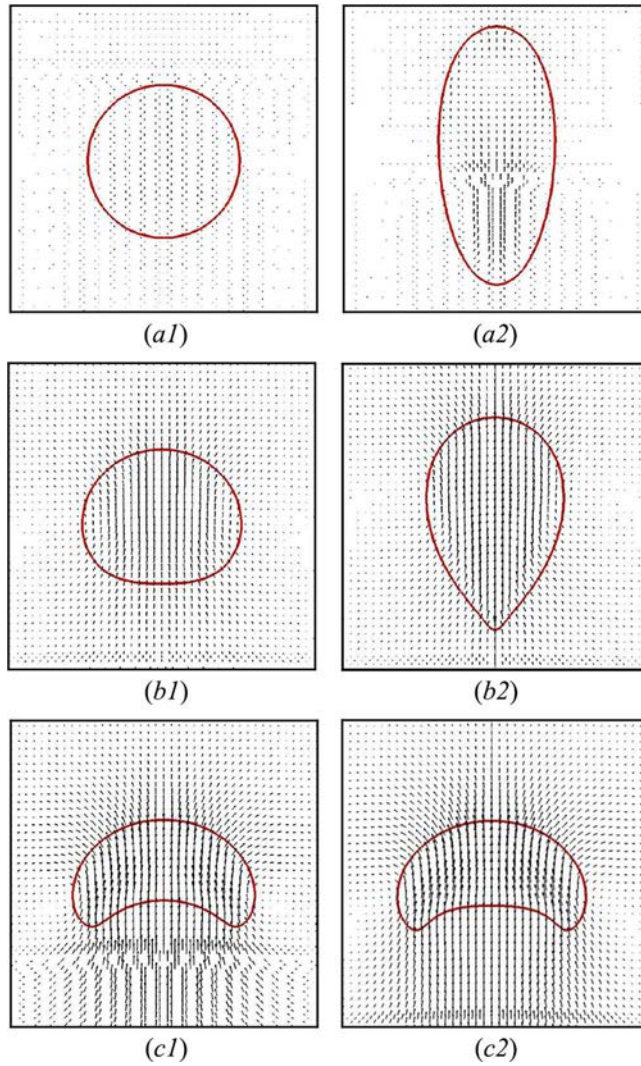
Figure 17. Terminal shapes and velocity fields of the bubble for different Eotvos (Eo) and electric Bond numbers (Bo_e) when $M = 10$ and $\lambda_\varepsilon = 5$: ($a1$) $Eo = 2$ and $Bo_e = 0$, ($a2$) $Eo = 2$ and $Bo_e = 10$, ($b1$) $Eo = 10$ and $Bo_e = 0$, ($b2$) $Eo = 10$ and $Bo_e = 10$, ($c1$) $Eo = 100$ and $Bo_e = 0$, ($c2$) $Eo = 100$ and $Bo_e = 10$.
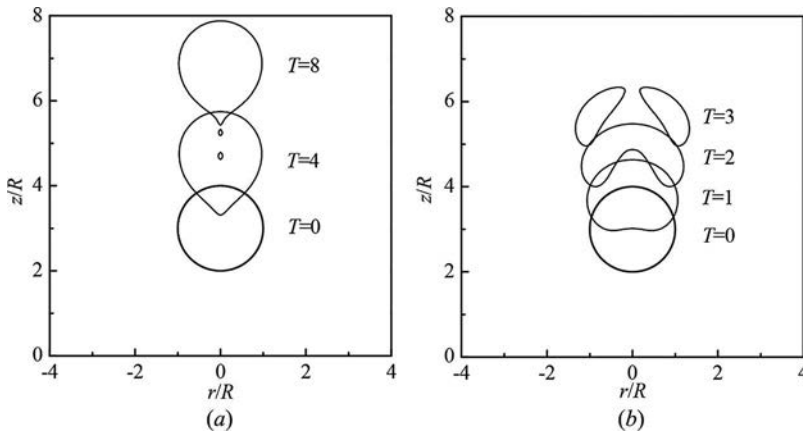

Figure 18. Evolution of the bubble shape with dimensionless time. (a) $M = 1000$, $Eo = 100$, $Bo_e = 20$, and $\lambda_\varepsilon = 5$; (b) $M = 0.1$, $Eo = 100$, $Bo_e = 10$, and $\lambda_\varepsilon = 5$.

When Eotvos number is large enough, some special phenomena appear when the bubble is subjected to an electric field. The bubble with $Eo = 100$ will be taken as an example in the following discussion. In Figure 18a, when $M = 1,000$, $Eo = 100$, $Bo_e = 20$, and $\lambda_\varepsilon = 5$, the bubble bottom becomes more and more acute and two satellite bubbles are produced at $T = 8$. In addition, when the Morton number is small, the bubble in the electric field is not very stable and a modest electric field will tear the bubble apart. Figure 18b shows that the bubble breaks up within a short time when $M = 0.1$, $Eo = 100$, $Bo_e = 10$, and $\lambda_\varepsilon = 5$.

5. Conclusions

The bubble dynamics in the gravitational and electric fields are studied with a proposed VOF+LS+SPP method based on the FLUENT software. This method proves to be accurate enough by comparing with previous simulation results. Then, the effects of electric Bond number (Bo_e), permittivity ratio (λ_ε), Morton number (M), and Eotvos number (Eo) on the bubble motion and deformation are systematically investigated.

Generally speaking, an additional uniform direct current electric field tends to elongate the bubble along the electric field direction and increase the bubble rising velocity. To be specific, however, the four dimensionless numbers still have distinguishing influences on bubble dynamics.

First, although a larger electric Bond number or permittivity ratio always leads to a larger bubble deformation and higher rising velocity, the electric Bond number has a greater influence on the bubble Reynolds number than permittivity ratio. In particular, when $\lambda_\varepsilon \geq 10$, the Reynolds number only increases a little with the increase of permittivity ratio. The laws are the same for all cases with different Morton and Eotvos numbers.

Second, the increase of Morton number decreases the bubble rising velocity. However, the bubble behaviors in the electric field are similar for different Morton numbers. The relative bubble Reynolds number changes a little with the variation of Morton number.

Third, the increase of Eotvos number increases the bubble rising velocity. The bubble behaviors in the electric field are totally different for different Eotvos numbers. The relative bubble Reynolds number decreases obviously with the increase of Eotvos number.

Funding

References

[1] J. R. Grace, Shapes and Velocities of Bubbles Rising in Infinite Liquids, *Trans. Inst. Chem. Eng.*, vol. 51, pp. 116–120, 1973.
[2] D. Bhaga and M. E. Weber, Bubbles in Viscous Liquids: Shapes, Wakes and Velocities, *J. Fluid Mech.*, vol. 105, pp. 61–85, 1981.
[3] M. M. Wu and M. Gharib, Experimental Studies on the Shape and Path of Small Air Bubbles Rising in Clean Water, *Phys. Fluids (1994-Present)*, vol. 14, pp. L49–L52, 2002.
[4] L. Liu, H. J. Yan, and G. J. Zhao, Experimental Studies on the Shape and Motion of Air Bubbles in Viscous Liquids, *Exp. Thermal Fluid Sci.*, vol. 62, pp. 109–121, 2015.
[5] M. Van Sint Annaland, N. G. Deen, and J. A. M. Kuipers, Numerical Simulation of Gas Bubbles Behaviour Using a Three-Dimensional Volume of Fluid Method, *Chem. Eng. Sci.*, vol. 60, pp. 2999–3011, 2005.
[6] L. Amaya-Bower and T. Lee, Single Bubble Rising Dynamics for Moderate Reynolds Number Using Lattice Boltzmann Method, *Comput. Fluids*, vol. 39, pp. 1191–1207, 2010.
[7] D. M. Nie, J. Z. Lin, L. M. Qiu, and X. B. Zhang, *Lattice Boltzmann Simulation of Multiple Bubbles Motion under Gravity, Abstract and Applied Analysis*, pp. 1–12, Hindawi Publishing Corporation, Cairo, Egypt, 2015.
[8] Z. Yu and L. S. Fan, Direct Simulation of the Buoyant Rise of Bubbles in Infinite Liquid Using Level Set Method, *Can. J. Chem. Eng.*, vol. 86, pp. 267–275, 2008.

[9] N. Balcázar, O. Lehmkuhl, L. Jofre, and A. Oliva, Level-Set Simulations of Buoyancy-Driven Motion of Single and Multiple Bubbles, *Int. J. Heat Fluid Flow*, vol. 56, pp. 91–107, 2015.

[10] J. S. Hua, J. F. Stene, and P. Lin, Numerical Simulation of 3D Bubbles Rising in Viscous Liquids Using a Front Tracking Method, *J. Comput. Phys.*, vol. 227, pp. 3358–3382, 2008.

[11] M. Ohta, T. Imura, Y. Yoshida, and M. Sussman, A Computational Study of the Effect of Initial Bubble Conditions on the Motion of A Gas Bubble Rising in Viscous Liquids, *Int. J. Multiphase Flow*, vol. 31, pp. 223–237, 2005.

[12] S. U. Sarnobat, S. Rajput, D. D. Bruns, D. W. DePaoli, C. S. Daw, and K. Nguyen, The Impact of External Electrostatic Fields on Gas-Liquid Bubbling Dynamics, *Chem. Eng. Sci.*, vol. 59, pp. 247–258, 2004.

[13] W. Dong, R. Y. Li, H. L. Yu, and Y. Y. Yan, An Investigation of Behaviours of a Single Bubble in a Uniform Electric Field, *Exp. Thermal Fluid Sci.*, vol. 30, pp. 579–586, 2006.

[14] S. Di Bari and A. J. Robinson, Adiabatic Bubble Growth in Uniform DC Electric Fields, *Exp. Thermal Fluid Sci.*, vol. 44, pp. 114–123, 2013.

[15] H. B. Zhang, Y. Y. Yan, and Y. Q. Zu, Numerical Modelling of EHD Effects on Heat Transfer and Bubble Shapes of Nucleate Boiling, *Appl. Math. Model*, vol. 34, pp. 626–638, 2010.

[16] S. Shin, Direct Numerical Simulation of Rising Bubble Interaction with Free Surface Using Level Contour Reconstruction Method, *J. Mech. Sci. Technol.*, vol. 26, pp. 3141–3148, 2012.

[17] P. Di Marco, R. Kurimoto, G. Saccone, K. Hayashi, and A. Tomiyama, Bubble Shape under the Action of Electric Forces, *Exp. Thermal Fluid Sci.*, vol. 49, pp. 160–168, 2013.

[18] S. Sunder and G. Tomar, Numerical Simulations of Bubble Formation from Submerged Needles under Non-Uniform Direct Current Electric Field, *Phys. Fluids (1994-Present)*, vol. 25, pp. 102104, 2013.

[19] S. Sunder and G. Tomar, Numerical Simulations of Bubble Formation from a Submerged Orifice and a Needle: The Effects of an Alternating Electric Field, *Eur. J. Mech. B Fluids*, vol. 56, pp. 97–109, 2016.

[20] S. Mählmann and D. T. Papageorgiou, Buoyancy-Driven Motion of a Two-Dimensional Bubble or Drop through a Viscous Liquid in the Presence of a Vertical Electric Field, *Theor. Comput. Fluid Dyn.*, vol. 23, pp. 375–399, 2009.

[21] Q. Yang, Y. Liu, B. Q. Li, and Y. C. Ding, *Effect of Electric Field on a 3D Rising Bubble in Viscous Fluids, Proceedings of the ASME 2013 Heat Transfer Summer Conference*, pp. 1–8, Minneapolis, MN, USA, 2013.

[22] Q. Z. Yang, B. Q. Li, J. Y. Shao, and Y. C. Ding, A Phase Field Numerical Study of 3D Bubble Rising in Viscous Fluids under an Electric Field, *Int. J. Heat Mass Transfer*, vol. 78, pp. 820–829, 2014.

[23] T. Wang, H. X. Li, Y. F. Zhang, and D. X. Shi, Numerical Simulation of Bubble Dynamics in a Uniform Electric Field by the Adaptive 3D-VOSET Method, *Numer. Heat Transfer Part A Appl.*, vol. 67, pp. 1352–1369, 2015.

[24] T. Wang, H. X. Li, and J. F. Zhao, Three-Dimensional Numerical Simulation of Bubble Dynamics in Microgravity under the Influence of Nonuniform Electric Fields, *Microgravity Sci. Technol.*, vol. 28, pp. 133–142, 2016.

[25] A. L. Zhang, Y. N. Wang, D. L. Sun, S. Yu, B. Yu, and Y. Li, Development of a VOF+LS+SPP Method Based on FLUENT for Simulating Bubble Behaviors in the Electric Field, *Numer. Heat Transfer, Part B Fundamentals*, vol. 71, pp. 186–201, 2017.

[26] J. R. Melcher and G. I. Taylor, Electrohydrodynamics: A Review of the Role of Interfacial Shear Stresses, *Annu. Rev. Fluid Mech.*, vol. 1, pp. 111–146, 1969.

[27] D. L. Youngs, Time-Dependent Multi-Material Flow with Large Fluid Distortion, in Morton, K. W. and Bianes M. J. eds., *Numerical Method for Fluid Dynamics*, pp. 273–285, Academic Press, New York, 1982.

[28] S. Osher and J. A. Sethian, Fronts Propagating with Curvature-Dependent Speed: Algorithms Based on Hamilton-Jacobi Formulations, *J. Comput. Phys.*, vol. 79, pp. 12–49, 1988.

[29] J. U. Brackbill, D. B. Kothe, and C. Zemach, A Continuum Method for Modeling Surface Tension, *J. Comput. Phys.*, vol. 100, pp. 335–354, 1992.

[30] J. D. Sherwood, Breakup of Fluid Droplets in Electric and Magnetic Fields, *J. Fluid Mech.*, vol. 188, pp. 133–146, 1988.

[31] J. S. Hua, L. K. Lim, and C. H. Wang, Numerical Simulation of Deformation/Motion of a Drop Suspended in Viscous Liquids under Influence of Steady Electric Fields, *Phys. Fluids (1994-Present)*, vol. 20, pp. 113302, 2008.

[32] Y. Lin, P. Skjetne, and A. Carlson, A Phase Field Model for Multiphase Electro-Hydrodynamic Flow, *Int. J. Multiphase Flow*, vol. 45, pp. 1–11, 2012.

[33] Y. Lin, Two-Phase Electro-Hydrodynamic Flow Modeling by a Conservative Level Set Model, *Electrophoresis*, vol. 34, pp. 736–744, 2013.